molecular pharmaceutics

Article

pubs.acs.org/molecularpharmaceutics

# Positron Emission Tomography and Optical Imaging of Tumor CD105 Expression with a Dual-Labeled Monoclonal Antibody

Yin Zhang,[†,‡] Hao Hong,[‡,§] Jonathan W. Engle,[†] Yunan Yang,[§] Charles P. Theuer,[∥] Todd E. Barnhart,[†] and Weibo Cai*[,†,§,⊥]

[†]Department of Medical Physics and [§]Department of Radiology, University of Wisconsin—Madison, Madison, Wisconsin, United States

[∥]TRACON Pharmaceuticals, Inc., San Diego, California, United States

[⊥]University of Wisconsin Carbone Cancer Center, Madison, Wisconsin, United States

**ABSTRACT:** CD105 (endoglin) is an independent prognostic marker for poor prognosis in >10 solid tumor types, including breast cancer. The goal of this study was to develop a CD105-specific agent for both positron emission tomography (PET) and near-infrared fluorescence (NIRF) imaging, which can have potential clinical applications in diagnosis and imaged-guided surgery of breast cancer. TRC105, a chimeric anti-CD105 monoclonal antibody, was labeled with both a NIRF dye (i.e., 800CW) and $^{64}$Cu to yield $^{64}$Cu-NOTA−TRC105−800CW. Flow cytometry analysis revealed no difference in CD105 binding affinity/specificity between TRC105 and NOTA−TRC105−800CW. Serial PET imaging revealed that the 4T1 murine breast tumor uptake of $^{64}$Cu-NOTA−TRC105−800CW was 5.2 ± 2.7, 11.0 ± 1.4, and 13.0 ± 0.4% ID/g at 4, 24, and 48 h postinjection respectively. Tumor uptake as measured by ex vivo NIRF imaging exhibited a good linear correlation with the % ID/g values obtained from PET ($R$ = 0.74). Biodistribution data were consistent with the PET/NIRF findings. Blocking experiments, control studies with dual-labeled cetuximab (an isotype-matched control antibody), and histology confirmed the CD105 specificity of $^{64}$Cu-NOTA−TRC105−800CW. Successful PET/NIRF imaging of CD105 expression warrants further investigation and clinical translation of dual-labeled TRC105-based imaging agents.

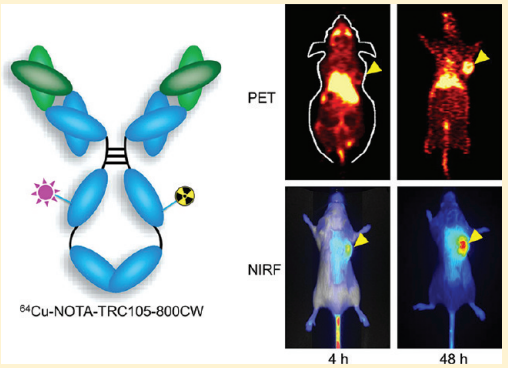


**KEYWORDS:** *CD105/endoglin, positron emission tomography (PET), near-infrared fluorescence (NIRF), tumor angiogenesis, TRC105, $^{64}$Cu, breast cancer*

## INTRODUCTION

One of the key requirements during tumor development is angiogenesis, the formation of new blood vessels, without which a tumor cannot grow beyond a few millimeters in diameter.[1−3] Angiogenesis is important not only during the rapidly growing macroscopic stage but also in the microscopic premalignant phase of neoplastic progression. Tremendous effort has been devoted to angiogenesis-related research over the past decade, particularly those involving noninvasive molecular imaging techniques.[4] Integrin $\alpha_v\beta_3$ and vascular endothelial growth factor receptors (VEGFRs), for which several tracers have entered clinical investigation,[5−9] are two of the most intensively studied angiogenesis-related targets. Another attractive target related to tumor angiogenesis that deserves more investigation is CD105 (also called "endoglin"), a 180 kDa disulfide-linked homodimeric transmembrane protein.[10−12]

Considered to be a suitable marker for evaluating tumor angiogenesis,[13,14] CD105 is overexpressed on vascular endothelial cells of tissues undergoing angiogenesis (e.g., tumors or regenerating/inflamed tissues).[15,16] Clinically, high CD105 expression correlates with poor prognosis in more than 10 solid tumor types.[10,11] Mounting preclinical and clinical data over the past decade clearly supported the role of CD105 as a marker for tumor angiogenesis, underscoring its emerging clinical potential as a prognostic, diagnostic, and therapeutic target for cancer detection and therapy. Surprisingly, molecular imaging of CD105 expression is understudied to date and literature reports on CD105 imaging are all based on labeling of anti-CD105 antibodies.[14,16−21]

Each molecular imaging modality has its advantages and disadvantages.[22] For example, it is difficult to accurately quantify fluorescence signal in living subjects, particularly in deep tissues. Positron emission tomography (PET) has very high sensitivity but suffers from relatively poor spatial resolution. Recently, a common approach in molecular imaging research is to combine methods that exhibit high spatial resolution with those having high detection sensitivity. Dual-modality imaging agents which combine the high resolution near-infrared fluorescence (NIRF) imaging with excellent sensitivity and quantitative capability of radionuclide-based techniques, such as PET, would be of great use in the clinic.

**Received:** November 20, 2011
**Revised:** January 5, 2012
**Accepted:** January 19, 2012
**Published:** January 31, 2012

PET/NIRF imaging, with a single contrast agent, can offer synergistic advantages over each modality alone.[23] In vivo optical imaging in the NIR (700−900 nm) region is optimal, since the absorbance spectra for all biomolecules reach minima thus providing a clear optical window for small animal studies and limited clinical scenarios (e.g., breast imaging, endoscopy, intraoperative visualization, etc.).[24,25] In addition to better tissue penetration of light, there is also significantly less background signal due to tissue autofluorescence in the NIR window. One scenario where such a dual-modality PET/NIRF agent is particularly useful is when an initial whole-body PET scan can be carried out to identify the location of tumor(s), and NIRF imaging can be subsequently used to provide a "roadmap" for the physicians during surgery.

TRC105, a human/murine chimeric IgG1 monoclonal antibody (mAb) which binds to both human and murine CD105 with high avidity, has completed a multicenter phase 1 first-in-human dose-escalation trial.[26] Multiple phase 2 therapy trials are underway in patients with various solid tumor types (e.g., breast, prostate, bladder, ovarian, and liver cancer). In this study, we conjugated TRC105 with both $^{64}$Cu (a PET isotope with a $t_{1/2}$ of 12.7 h) and a NIRF dye, IRDye 800CW (Ex, 778 nm; Em, 806 nm) and investigated the dual-labeled agent for PET/NIRF imaging of tumor CD105 expression in a mouse model of breast cancer.

## EXPERIMENTAL SECTION

**Reagents.** TRC105 was provided by TRACON Pharmaceuticals Inc. (San Diego, CA). Cetuximab (a human/murine chimeric IgG1 mAb that binds to human epidermal growth factor receptor [EGFR] but does not cross-react with murine EGFR[20]) was from Bristol-Meyers Squibb Company (Princeton, NJ). AlexaFluor488- and Cy3-labeled secondary antibodies were purchased from Jackson Immunoresearch Laboratories, Inc. (West Grove, CA). 2-*S*-(4-Isothiocyanatobenzyl)-1,4,7-triazacyclononane-1,4,7-triacetic acid (*p*-SCN-Bn-NOTA) and Chelex 100 resin (50−100 mesh) were purchased from Macrocyclics, Inc. (Dallas, TX) and Sigma-Aldrich (St. Louis, MO), respectively. IRDye 800CW-NHS (NHS denotes *N*-hydroxysuccinimide) ester was acquired from LI-COR Biosciences Co. (Lincoln, NE). Water and all buffers were of Millipore grade and pretreated with Chelex 100 resin to ensure that the aqueous solution was heavy metal-free. PD-10 columns were purchased from GE Healthcare (Piscataway, NJ). All other reaction buffers and chemicals were from Thermo Fisher Scientific (Fair Lawn, NJ).

**Cell Lines and Animal Model.** 4T1 murine breast cancer cells and human umbilical vein endothelial cells (HUVECs) were purchased from the American Type Culture Collection (ATCC, Manassas, VA). 4T1 cells were cultured in RPMI 1640 medium (Invitrogen, Carlsbad, CA) with 10% fetal bovine serum and incubated at 37 °C with 5% $CO_2$. HUVECs were cultured in M-200 medium (Invitrogen, Carlsbad, CA) with 1× low serum growth supplement (Cascade Biologics, Portland, OR) and incubated at 37 °C with 5% $CO_2$. Cells were used for in vitro and in vivo experiments when they reached ∼75% confluence.

All animal studies were conducted under a protocol approved by the University of Wisconsin Institutional Animal Care and Use Committee. For the 4T1 tumor model, four- to five-week-old female Balb/c mice were purchased from Harlan (Indianapolis, IN) and tumors were established by subcutaneously injecting $2 \times 10^6$ cells, suspended in 100 μL of 1:1 mixture of RPMI 1640 and Matrigel (BD Biosciences, Franklin lakes, NJ), into the front flank of mice.[27] Tumor sizes were monitored every other day, and mice were used for in vivo experiments when the diameter of tumors reached 5−8 mm (typically 1−2 weeks after inoculation).

**NOTA/800CW Conjugation and $^{64}$Cu-Labeling of Antibodies.** NOTA conjugation was carried out at pH 9.0, with the reaction ratio of *p*-SCN-Bn-NOTA:mAb being 25:1. NOTA−TRC105 and NOTA−cetuximab were purified using PD-10 columns with phosphate buffered saline (PBS) as the mobile phase. After NOTA conjugation, a molar ratio of 2:1 was used for the reactions between 800CW-NHS and NOTA−TRC105 or NOTA−cetuximab. The pH value of the reaction mixtures was adjusted to 8.5 with 0.1 M $Na_2CO_3$. After continuous stirring of the reaction mixture at room temperature (rt) for 2 h, NOTA−TRC105−800CW and NOTA−cetuximab−800CW were purified with PD-10 columns.

For radiolabeling, $^{64}CuCl_2$ (74 MBq) was diluted in 300 μL of 0.1 M sodium acetate buffer (pH 6.5) and added to 50 μg of NOTA−TRC105−800CW or NOTA−cetuximab−800CW. The reaction mixture was incubated for 30 min at 37 °C with constant shaking. $^{64}$Cu-NOTA−TRC105−800CW and $^{64}$Cu-NOTA−cetuximab−800CW were purified using PD-10 columns with PBS as the mobile phase. The radioactive fractions containing $^{64}$Cu-NOTA−TRC105−800CW or $^{64}$Cu-NOTA−cetuximab−800CW were collected and passed through a 0.2 μm syringe filter for in vivo experiments.

**Flow Cytometry.** The immunoreactivity of TRC105 and NOTA−TRC105−800CW to HUVECs (high CD105 expression[20,28]) and 4T1 cells (CD105-negative[20]) were evaluated by fluorescence-activated cell sorting (FACS) analysis. Briefly, cells were harvested and suspended in cold PBS (pH 7.4) with 2% bovine serum albumin at a concentration of $5 \times 10^6$ cells/mL. The cells were incubated with various concentrations of TRC105 or NOTA−TRC105−800CW (1, 5, or 15 μg/mL) for 30 min at rt, washed three times with cold PBS, and centrifuged at 1,000 rpm for 5 min. The cells were then incubated with AlexaFluor488-labeled goat anti-human IgG (5 μg/mL) for 30 min at rt. Afterward, the cells were washed and analyzed by FACS using a BD FACSCalibur 4-color analysis cytometer, which is equipped with 488 nm and 633 nm lasers (Becton-Dickinson, San Jose, CA) and FlowJo analysis software (Tree Star, Inc., Ashland, OR).

**Imaging and Biodistribution Studies.** Hair on the back of each mouse was removed before imaging studies to reduce light scattering. PET scans were performed using an Inveon microPET/microCT rodent model scanner (Siemens Medical Solutions USA, Inc.). Each 4T1 tumor-bearing mouse was intravenously injected with 5−10 MBq of $^{64}$Cu-NOTA−TRC105−800CW or $^{64}$Cu-NOTA−cetuximab−800CW, adjusted to contain 300 picomoles (pmol) of 800CW using "cold" NOTA−TRC105−800CW or NOTA−cetuximab−800CW. Five-minute static PET scans were performed at various time points postinjection (p.i.). The images were reconstructed using a maximum a posteriori (MAP) algorithm, with no attenuation or scatter correction. Region-of-interest (ROI) analysis of each PET scan was performed using vendor software (Inveon Research Workplace [IRW]) on decay-corrected whole-body images as described previously,[20] to calculate the percentage injected dose per gram of tissue (% ID/g) values for the 4T1 tumor and several major organs.

Blocking studies were carried out to evaluate the CD105 specificity of $^{64}$Cu-NOTA−TRC105−800CW in vivo, where a group of 3 mice was each injected with 2 mg of TRC105 within 2 h before $^{64}$Cu-NOTA−TRC105−800CW administration.

A subset of mice was also subjected to CT scans, with a voxel resolution of 210 $\mu$m. Fiducial markers were used for coregistration, and images were reconstructed using the vendor software (Inveon Acquisition Workshop; Siemens). The CT and PET data sets were registered via rigid registration in IRW.

Immediately after PET scanning, the mice were imaged in a Pearl Impulse scanner (LI-COR, Inc., Lincoln, NE) using the 800 nm/white channels. Longitudinal NIRF images for each mouse were normalized with common minimum and maximum values. Using vendor software, ROIs were drawn on the 4T1 tumors and the average signal intensity (presented as mean ± SD in the unit of counts/s/mm$^2$) within the ROI was used for subsequent quantitative analysis.

After the last in vivo PET/NIRF imaging at 48 h p.i., blood, 4T1 tumor, and major organs/tissues were harvested and imaged ex vivo with both scanners to validate the in vivo findings. Biodistribution studies were also carried out to confirm that the quantitative tracer uptake values based on PET imaging truly represented the radioactivity distribution in tumor-bearing mice. Blood, 4T1 tumor, and major organs/tissues were collected and wet-weighed. The radioactivity in the tissue was measured using a gamma-counter (Perkin-Elmer) and presented as % ID/g. The 4T1 tumor, liver, and spleen (i.e., tissues with significant uptake of $^{64}$Cu-NOTA−TRC105−800CW) were also frozen and sectioned for histological analysis.

**Histology.** Frozen tissue slices of 5 $\mu$m thickness were fixed with cold acetone for 10 min and dried in the air for 30 min. After rinsing with PBS and blocking with 10% donkey serum for 30 min at rt, the slices were incubated with TRC105 (2 $\mu$g/mL) for 1 h at 4 °C and visualized using AlexaFluor488-labeled goat anti-human IgG. The tissue slices were also stained for endothelial marker CD31 as described previously.[29,30] After washing with PBS, the slices were incubated with rat anti-mouse CD31 antibody (2 $\mu$g/mL) for 1 h, followed by Cy3-labeled donkey anti-rat IgG for 30 min. All images were acquired with a Nikon Eclipse Ti microscope.

**Statistical Analysis.** Quantitative data were expressed as mean ± SD. Means were compared using Student's $t$ test. $P$ values <0.05 were considered statistically significant. The % ID/g values based on PET were correlated with the quantitative data obtained from in vivo/ex vivo NIRF imaging. Applying a linear fit, the correlation coefficient ($R$) was calculated to measure the strength of the association between the PET and ex vivo NIRF data. $P$ values <0.05 were considered to have a statistically significant linear correlation between the two measurements.

## RESULTS

**In Vitro Investigation of NOTA−TRC105−800CW.** In the final antibody conjugates (NOTA−TRC105−800CW or NOTA−cetuximab−800CW), on average ~5 NOTA and ~0.9 800CW molecules were conjugated to each mAb based on UV measurements. Less than one 800CW per mAb will avoid any self-quenching due to close proximity of 800CW molecules, since fluorescence resonance energy transfer only occurs when two 800CW molecules are within 10 nm (about the size of an mAb). Such minimal NOTA/800CW conjugation of TRC105 did not alter its CD105 binding affinity, as evidenced by FACS analysis of HUVECs which express a high level of CD105 (Figure 1). No observable differences were found between TRC105 and NOTA−TRC105−800CW at 1 $\mu$g/mL or 5 $\mu$g/mL concentrations, both at nonsaturating conditions. On the other hand, neither TRC105 nor NOTA−TRC105−800CW bound to CD105-negative 4T1 cells, even at a much higher concentration of 15 $\mu$g/mL (Figure 1). Taken together, FACS analysis confirmed that NOTA and 800CW conjugation did not alter the antigen binding affinity or specificity of TRC105.

**$^{64}$Cu-Labeling.** $^{64}$Cu-labeling including final purification using PD-10 columns took 60 ± 10 min ($n$ = 10). The decay-corrected radiochemical yield was >85%, based on 25 $\mu$g of mAb conjugate (NOTA−TRC105−800CW or NOTA−cetuximab−800CW) per 37 MBq of $^{64}$Cu, and the radiochemical purity was >98%. The specific activity of both $^{64}$Cu-NOTA−TRC105−800CW and $^{64}$Cu-NOTA−cetuximab−800CW was about 1.3 GBq/mg protein, assuming complete recovery of the NOTA−mAb−800CW conjugate after size exclusion chromatography.

**Small Animal PET Imaging.** The time points of 4, 24, and 48 h p.i. were chosen for serial PET/NIRF scans after intravenous tracer injection based on our previous study, with the first time point in the initial tumor accumulation phase and the subsequent two time points within a plateau of 4T1 tumor uptake.[20] Coronal PET images that contain the 4T1 tumor are shown in Figure 2A, with the quantitative data obtained from ROI analysis and representative PET/CT fused images of a mouse at 48 h p.i. of $^{64}$Cu-NOTA−TRC105−800CW shown in Figure 3.

Due to better in vivo stability of the $^{64}$Cu-NOTA complex than $^{64}$Cu-DOTA (DOTA denotes 1,4,7,10-tetraazacyclododecane-1,4,7,10-tetraacetic acid), liver uptake of $^{64}$Cu-NOTA−TRC105−800CW was significantly lower at all time points examined than that observed for $^{64}$Cu-DOTA−TRC105 (which may have a certain degree of $^{64}$Cu-transchelation, thereby

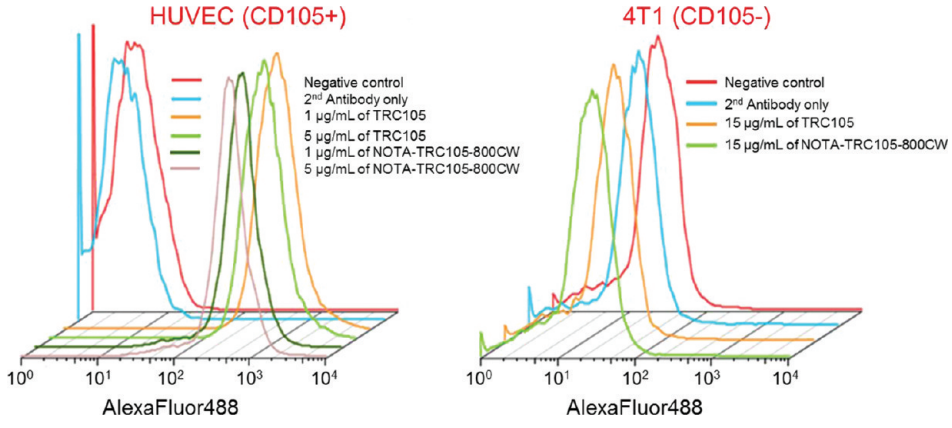


**Figure 1.** Flow cytometry analysis of TRC105 and NOTA−TRC105−800CW in HUVECs (CD105-positive) and 4T1 murine breast cancer cells (CD105-negative) at different concentrations. Data from control experiments are also shown.


dx.doi.org/10.1021/mp200592m | Mol. Pharmaceutics 2012, 9, 645−653

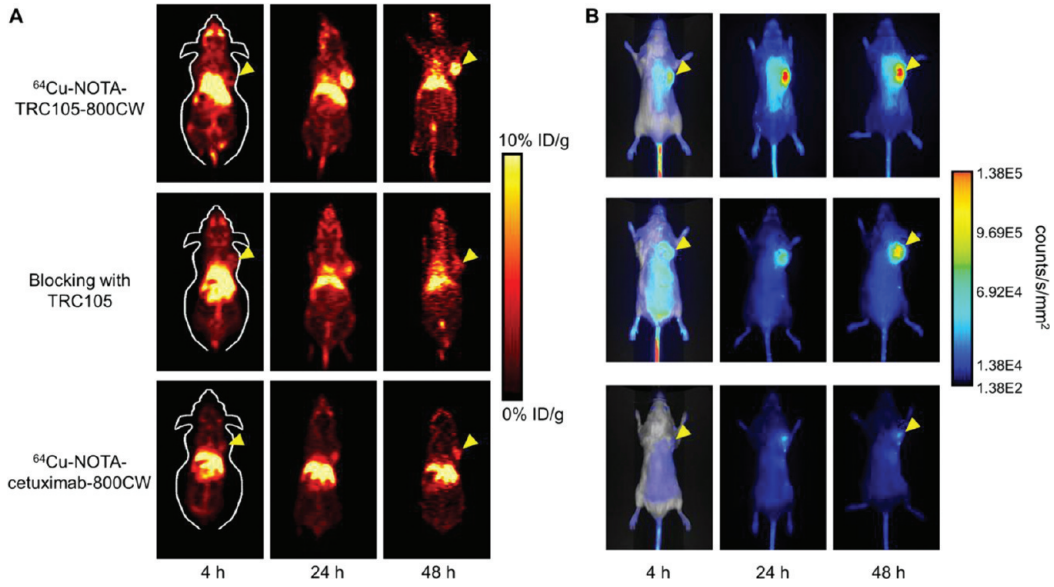


**Figure 2.** Serial in vivo PET/NIRF imaging of 4T1 tumor-bearing mice. (A) Coronal PET images at 4, 24, and 48 h postinjection of $^{64}$Cu-NOTA−TRC105−800CW, 2 mg of TRC105 before $^{64}$Cu-NOTA−TRC105−800CW (i.e., blocking), or $^{64}$Cu-NOTA−cetuximab−800CW. (B) Serial NIRF images of the same mice in (A). The amount of 800CW injected into each mouse was 300 pmol, and images are representative of each group of 3 mice. All images were acquired under the same condition and displayed at the same scale. The first image in each row is a merged image of the fluorescence signal and a photo of the mouse, while subsequent images in each row are fluorescence images only. Arrowheads indicate the 4T1 tumors in all cases.

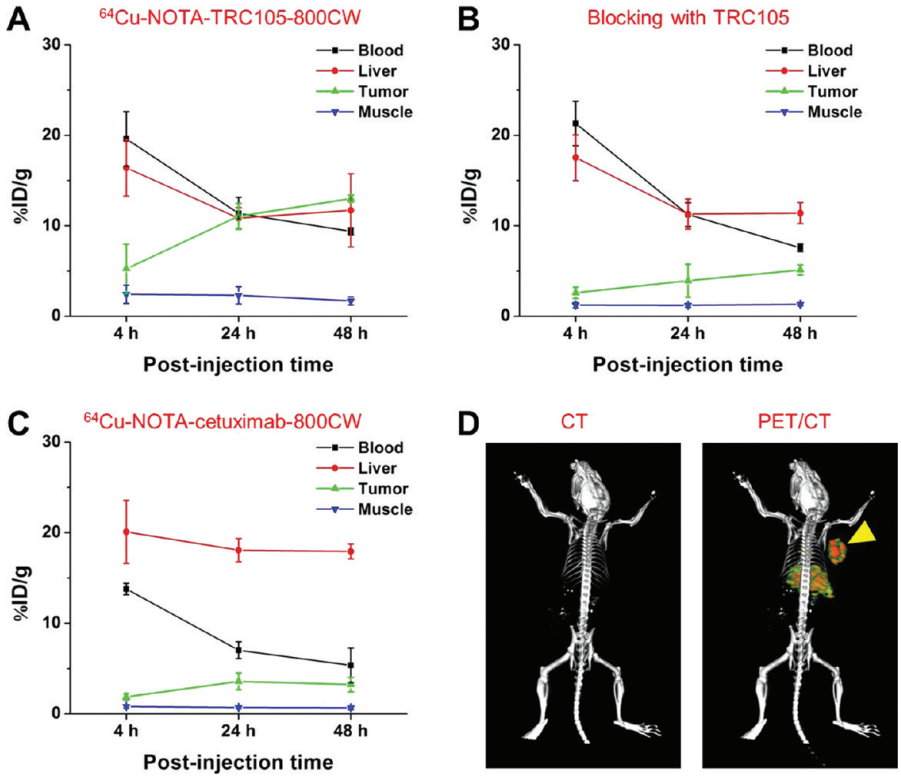


**Figure 3.** Quantitative analysis of the PET data. (A) Time−activity curves of the blood, liver, 4T1 tumor, and muscle upon intravenous injection of $^{64}$Cu-NOTA−TRC105−800CW into 4T1 tumor-bearing mice ($n$ = 3). (B) Time−activity curves of the blood, liver, 4T1 tumor, and muscle upon intravenous injection of $^{64}$Cu-NOTA−TRC105−800CW, after a blocking dose of TRC105, into 4T1 tumor-bearing mice ($n$ = 3). (C) Time−activity curves of the blood, liver, 4T1 tumor, and muscle upon intravenous injection of $^{64}$Cu-NOTA−cetuximab−800CW into 4T1 tumor-bearing mice ($n$ = 3). (D) Representative PET/CT images of a 4T1-tumor bearing mouse at 48 h postinjection of $^{64}$Cu-NOTA−TRC105−800CW.

increasing radioactivity accumulation in the liver) in our previous study in the same tumor model.[20] Meanwhile, blood pool activity was prominent at early time points (due to long circulation half-life of the antibody) which gradually declined over time. The liver uptake of $^{64}$Cu-NOTA−TRC105−800CW was 16.4 ± 3.1, 10.8 ± 1.1, and 11.7 ± 4.4% ID/g at 4, 24, and 48 h p.i. respectively, while the radioactivity in the blood was 19.6 ± 3.0, 11.4 ± 1.8, and 9.4 ± 0.4% ID/g at 4, 24, and 48 h


dx.doi.org/10.1021/mp200592m | Mol. Pharmaceutics 2012, 9, 645−653

p.i., respectively ($n$ = 3; Figure 3A). The 4T1 tumor uptake of $^{64}$Cu-NOTA−TRC105−800CW was clearly visible at as early as 4 h p.i. which reached a plateau at around 24 h p.i. (5.2 ± 2.7, 11.0 ± 1.4, and 13.0 ± 0.4% ID/g at 4, 24, and 48 h p.i. respectively; $n$ = 3; Figure 3A).

Administering a blocking dose of TRC105 two hours before $^{64}$Cu-NOTA−TRC105−800CW injection reduced the tumor uptake to background level ($P$ < 0.01 at 24 and 48 h p.i. when compared with mice injected with $^{64}$Cu-NOTA−TRC105−800CW alone; Figures 2A, 3B), which clearly indicated CD105 specificity of the tracer in vivo. Radioactivity in the blood was 21.3 ± 2.5, 11.2 ± 1.3, and 7.6 ± 0.4% ID/g at 4, 24, and 48 h p.i. respectively ($n$ = 3), and liver uptake was 17.5 ± 2.5, 11.3 ± 1.6, and 11.4 ± 1.1% ID/g at 4, 24, and 48 h p.i. respectively ($n$ = 3), slightly higher than that of mice injected with $^{64}$Cu-NOTA−TRC105−800CW alone at 4 h p.i., but similar at the time points of 24 and 48 h p.i.

To further investigate the CD105 specificity of $^{64}$Cu-NOTA−TRC105−800CW, $^{64}$Cu-NOTA−cetuximab−800CW was used as an isotype-matched control. Since both TRC105 and cetuximab are human/murine chimeric IgG1 mAbs and cetuximab does not cross-react with murine tissues, it serves as an ideal control for investigating tracer uptake in the tumor due to passive targeting only (i.e., the enhanced permeability and retention effect[31,32]). As can be seen in Figures 2A and 3C, the 4T1 tumor uptake of $^{64}$Cu-NOTA−cetuximab−800CW is at the background level (<4% ID/g) and significantly lower than that of $^{64}$Cu-NOTA−TRC105−800CW at all time points examined ($P$ < 0.05 at 4 h p.i.; $P$ < 0.01 at 24 and 48 h p.i.; $n$ = 3), which again confirms the CD105 specificity of $^{64}$Cu-NOTA−TRC105−800CW in vivo.

**In Vivo NIRF Imaging.** In vivo NIRF imaging of 4T1 tumor-bearing mice was carried out at 4, 24, and 48 h p.i. immediately after the PET scans, with representative images from each group shown in Figure 2B. Tumor contrast was observed for $^{64}$Cu-NOTA−TRC105−800CW as early as 4 h p.i. Subsequently, the tumor uptake continued to increase and plateaued at 24 h p.i., suggesting specific interaction between the antibody (i.e., TRC105) and its antigen (i.e., CD105). Quantitative ROI analysis yielded average tumor signal intensity of $7.11 \times 10^4 \pm 0.86 \times 10^4$, $1.56 \times 10^5 \pm 1.54 \times 10^4$, and $1.19 \times 10^5 \pm 2.41 \times 10^4$ counts/s/mm$^2$ at 4, 24, and 48 h p.i., respectively ($n$ = 3; Figure 4A). Preinjection of 2 mg of TRC105 per mouse before $^{64}$Cu-NOTA−TRC105−800CW administration resulted in tumor signal intensity of $4.04 \times 10^4 \pm 1.20 \times 10^4$, $8.97 \times 10^4 \pm 0.66 \times 10^4$, and $7.75 \times 10^4 \pm 1.36 \times 10^4$ counts/s/mm$^2$ at 4, 24, and 48 h p.i., respectively ($n$ = 3; Figure 4A; $P$ < 0.05 at 24 and 48 h p.i. when compared to $^{64}$Cu-NOTA−TRC105−800CW). Tumor signal intensity of $^{64}$Cu-NOTA−cetuximab−800CW was very low (<$2.5 \times 10^4$ counts/s/mm$^2$) at all time points examined. Taken together, the NIRF imaging results are in good agreement with the PET findings, both confirming CD105 specificity of $^{64}$Cu-NOTA−TRC105−800CW in vivo.

**Ex Vivo Imaging and Biodistribution Studies.** All mice were euthanized after the last PET scans at 48 h p.i. Major organs were subjected to both NIRF and PET imaging ex vivo (Figure 4C), which corroborated each other and are in accordance with the in vivo PET/NIRF images. Quantitative data from ROI analysis of major tissues, based on ex vivo NIRF imaging, are shown in Figure 4B. Excellent tumor contrast was observed in mice injected with $^{64}$Cu-NOTA−TRC105−800CW, but not the other two groups. Fluorescence signal intensity in the 4T1 tumor based on in vivo NIRF imaging ($1.19 \times 10^5 \pm 2.41 \times 10^4$ counts/s/mm$^2$ at 48 h p.i.; Figure 4A) was only slightly lower than that based on ex vivo NIRF imaging ($1.31 \times 10^5 \pm 1.58 \times 10^4$ counts/s/mm$^2$ at 48 h p.i.; Figure 4B), which confirmed that imaging in the NIR window was suitable for superficial tissues/tumors with little signal attenuation. Linear correlation between the ex vivo NIRF data and PET % ID/g values, using a total of 9 data points (4T1 tumor at 48 h p.i. for three groups of mice with three mice per group), gave a statistically significant ($P$ = 0.02) linear correlation with an $R$ value of 0.74 (Figure 4D), which indicated that NIRF imaging can give quite accurate quantitative results in ex vivo settings.

Biodistribution data at 48 h p.i. showed that 4T1 tumor uptake of $^{64}$Cu-NOTA−TRC105−800CW was higher than that of all organs in mice (Figure 5A), thereby providing excellent contrast. Preinjection of a blocking dose of TRC105 led to a significant decrease in 4T1 tumor uptake of $^{64}$Cu-NOTA−TRC105−800CW ($P$ < 0.05; $n$ = 3; Figure 5A), corroborating the in vivo PET findings. A comparison of the biodistribution data between the two tracers revealed that uptake of $^{64}$Cu-NOTA−cetuximab−800CW was significantly higher than that of $^{64}$Cu-NOTA−TRC105−800CW in the liver but much lower in the 4T1 tumor (Figure 5B), where significantly higher tumor uptake was observed for $^{64}$Cu-NOTA−TRC105−800CW due to CD105 binding ($P$ < 0.05; $n$ = 3). Overall, the quantification results obtained from biodistribution studies and PET scans matched very well, confirming that quantitative ROI analysis of noninvasive PET scans truly reflected tracer distribution in vivo.

**Histology.** CD105/CD31 costaining of various tissues revealed that CD105 expression in the 4T1 tumor was primarily on the tumor vasculature, as evidenced by excellent colocalization of CD105 and CD31 staining and little observable fluorescence signal on the 4T1 tumor cells (Figure 6). CD105 is only expressed on actively proliferating endothelial cells, thus mature vessels have significantly lower CD105 expression (indicated by arrowheads in Figure 6) than in the neovasculature. Since tumor vasculature is more actively proliferating in the peripheral region than in the center, tumor uptake of $^{64}$Cu-NOTA−TRC105−800CW is heterogeneous (i.e., higher in the peripheral region and lower in the tumor center).

CD105 staining of mouse liver and spleen both gave very low signals, indicating that these tissues do not have a significant level of CD105 expression. Thus, uptake of $^{64}$Cu-NOTA−TRC105−800CW in the liver was largely unrelated to CD105 binding and more likely attributed to nonspecific capture by the reticuloendothelial system (RES) and hepatic clearance of the tracer. Taken together, the ex vivo findings corroborated the in vivo data of $^{64}$Cu-NOTA−TRC105−800CW, warranting further investigation and applications of this tracer.

## ■ DISCUSSION

In this study, we have successfully developed a dual-labeled tracer for both PET and NIRF imaging of tumor CD105 expression, which can have potential applications in many clinical situations such as lesion detection (with PET imaging) and image-guided surgery (with NIRF imaging). The incorporation of two imaging labels on a single targeting agent (e.g., TRC105), where both labels were conjugated at a minimal level thereby exhibiting no appreciable effect on the antigen binding affinity/specificity as demonstrated in our study, is more advantageous than single modality imaging from

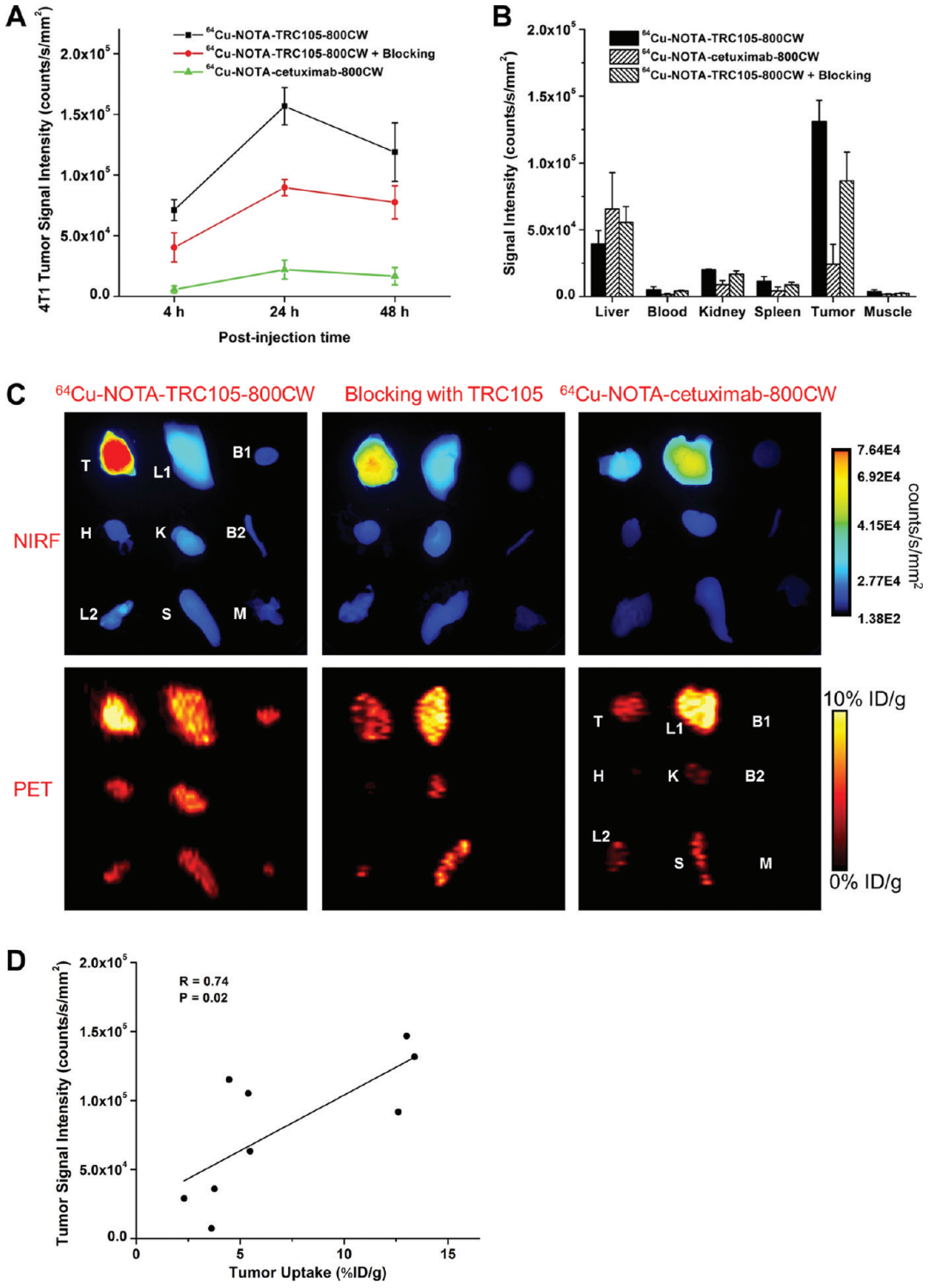


**Figure 4.** Quantification of NIRF signal intensity and correlation with PET data. (A) Signal intensity of the 4T1 tumor in the 3 groups of mice, based on in vivo NIRF imaging. (B) Signal intensity of the 4T1 tumor and major organs in the 3 groups of mice, based on ex vivo NIRF imaging at 48 h postinjection. (C) Ex vivo NIRF and PET imaging of the 4T1 tumor and major organs at 48 h postinjection of each tracer. Images are representative of 3 mice per group: T, 4T1 tumor; L1, liver; B1, blood; H, heart; K, kidney; B2, bone; L2, lung; S, spleen; M, muscle. (D) Correlation of the ex vivo NIRF signal intensity in all 4T1 tumor-bearing mice at 48 h postinjection with the % ID/g values based on ROI analysis of the PET data.

regulatory perspectives. The need for comprehensive toxicity/dosimetry studies in multiple animal species for only one agent instead of two separate agents (one for each imaging modality) can significantly reduce the development cost and facilitate future clinical translation of novel imaging agents.

Guiding surgery with molecularly targeted fluorescent agents has gained enormous interest over the past decade. Recently, a proof-of-principle study investigating the potential benefit of intraoperative tumor-specific fluorescence imaging in staging and debulking surgery for ovarian cancer using a systemically


dx.doi.org/10.1021/mp200592m | Mol. Pharmaceutics 2012, 9, 645–653

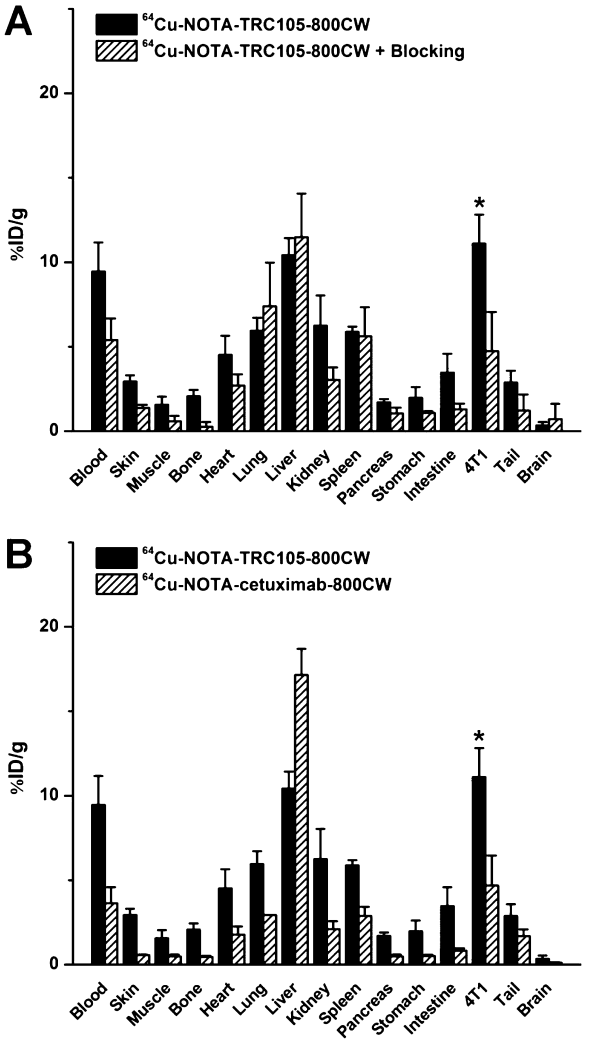


**Figure 5.** Biodistribution data at 48 h postinjection of each tracer. *: $P < 0.05$ ($n = 3$).

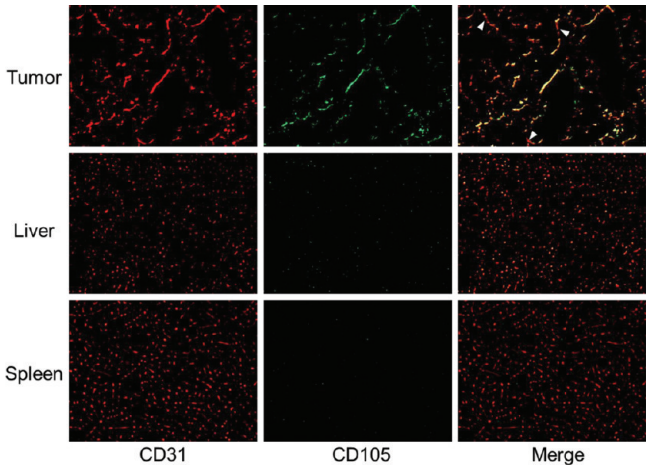


**Figure 6.** Immunofluorescence CD105/CD31 double-staining of the 4T1 tumor, liver, and spleen tissue sections. CD105 expression was high on newly formed blood vessels but not on mature vessels in the tumor, which exhibited predominantly CD31 staining (arrowheads). CD105 expression levels in the liver and spleen are much lower than in the tumor vessels. All images were acquired under the same conditions and displayed at the same scale. Magnification: 200×.

administered, targeted fluorescent agent (folate-FITC) was reported.[33] The use of a NIRF agent which has improved signal penetration in an image window with significantly less autofluorescence is expected to be more advantageous in surgery guidance, with the development of suitable intraoperative imaging systems. Immunohistochemistry of CD105 on tumor tissue is now the accepted standard approach for determining tumor microvessel density (MVD), a quantitative measure of tumor angiogenesis and an independent prognostic factor for survival in patients with many types of solid tumors.[11,12] Noninvasive imaging of CD105 expression with PET (essentially noninvasive measurement of whole-body MVD) and intraoperative imaging of CD105 (real-time MVD measurement), using a single agent such as the one developed in this study, has promising clinical potential in cancer diagnosis, in antiangiogenic drug development, in personalized medicine, and ultimately in day-to-day cancer patient management.

Our data showed that NOTA−TRC105−800CW specifically bound to CD105-positive HUVECs in vitro but not to CD105-negative 4T1 cells, even at a much higher concentration. Even though the 4T1 tumor cells are CD105 negative per se, they grow quickly when inoculated into mice, thus it has highly angiogenic tumor vasculature with prominent CD105 expression that is amenable for noninvasive imaging. The lack of CD105 expression on the tumor cells is one of the reasons why uptake of $^{64}$Cu-NOTA−TRC105−800CW in the 4T1 tumor is not as high as that of certain other antibody-based PET tracers,[29,34] which are targeting tumor cells instead of targeting tumor vasculature only. There are significantly fewer tumor vascular endothelial cells than tumor cells, which are the targets for most antibodies used for cancer imaging to date.

PET imaging has been widely used in clinical oncology for cancer staging and monitoring the therapeutic response.[35−39] In preclinical studies, $^{64}$Cu is one of the most widely used radioisotopes for immunoPET studies and there are many chelators available for $^{64}$Cu-labeling.[40] One of the key requirements for accurate PET imaging with $^{64}$Cu-labeled mAbs is that the tracer should be sufficiently stable during the imaging period, since the PET scanner detects the distribution of $^{64}$Cu instead of the mAb itself. Recently, it has been generally recognized that NOTA is one of the most suitable chelators for $^{64}$Cu-labeling,[41] even though several other chelators also exhibit similar in vitro stability and comparable tumor uptake. Compared to our previous study which focused on $^{64}$Cu-DOTA−TRC105,[20] the lower liver uptake and higher blood concentration of $^{64}$Cu-NOTA−TRC105−800CW confirmed better in vivo stability of $^{64}$Cu-NOTA over $^{64}$Cu-DOTA conjugated TRC105.

One key challenge in antibody labeling is to minimize the potential interference with its antigen binding affinity/specificity. There is only one lysine residue in each of the complementarity-determining regions (CDRs) of TRC105,[12] among a total of ∼1400 amino acid residues and ∼70 lysines in the antibody. Therefore, the possibility of NOTA or 800CW conjugation at the lysine residue within the CDR is very low, which was confirmed by FACS analysis at several non-antigen-saturating conditions (Figure 1). To confirm that tumor uptake of $^{64}$Cu-NOTA−TRC105−800CW measured by noninvasive PET/NIRF imaging techniques was indeed CD105 specific, various control experiments (e.g., blocking study with unconjugated TRC105, and the use of cetuximab as an isotype-matched control), in vitro/ex vivo studies (e.g., FACS and histological analysis), and biodistribution and ex vivo PET/NIRF imaging studies were all performed for validation purposes.


dx.doi.org/10.1021/mp200592m | Mol. Pharmaceutics 2012, 9, 645−653

The NIRF imaging aspect in this study represented the "best-case scenario" for optical imaging in that (1) the tumors were subcutaneously inoculated, thus tissue penetration of fluorescence signal was not a major issue; (2) the emission maximum of 800CW is 806 nm, which is in the optically clear NIR window; (3) mouse hair was removed before NIRF imaging, and the mouse skin is of light color; and (4) the use of laser excitation gave a stronger signal than other excitation sources. The statistically significant correlation between the ex vivo NIRF signal and PET-based % ID/g values indicated that imaging in the NIR window can provide (semi)quantitative information for subcutaneous tumors/tissues of light color. The accuracy of quantification is much lower for deeper tissues of darker color, as can be seen for the liver in both in vivo and ex vivo NIRF imaging (i.e., only weak fluorescence signal was observed in the liver even in the NIR window, despite the fact that liver uptake of $^{64}$Cu-NOTA–TRC105–800CW was prominent based on PET; Figures 2B, 4C). In clinical settings, NIRF imaging can be used for imaging tissues close to the surface of the skin (e.g., breast cancer imaging), tissues accessible by endoscopy (such as malignant lesions in the esophagus and colon), and intraoperative visualization (molecular imaging-guided surgery).

## CONCLUSION

Herein we report the development, characterization, and in vivo investigation of a dual-labeled agent (with $^{64}$Cu and a NIRF dye 800CW) for both PET and NIRF imaging of CD105 expression in a breast cancer model. Rapid, persistent, and CD105-specific uptake of $^{64}$Cu-NOTA–TRC105–800CW in the 4T1 tumor was observed with both imaging modalities, which was further validated by various in vitro, in vivo, and ex vivo control experiments. Tumor uptake based on ROI analysis of ex vivo NIRF imaging exhibited a linear correlation with the tumor % ID/g values measured with PET, confirming that imaging in the NIR window in small animal models can give accurate quantitative information in superficial (tumor) tissue of light color. Upon further optimization and development, such dual-labeled PET/NIRF agents can be translated into the clinic for both disease diagnosis and image-guided surgery, not only in breast cancer but also in other solid tumors types.

## AUTHOR INFORMATION

### Corresponding Author

*Departments of Radiology and Medical Physics, University of Wisconsin—Madison, Room 7137, 1111 Highland Ave, Madison, WI 53705-2275, USA. E-mail: wcai@uwhealth.org. Phone: 608-262-1749. Fax: 608- 265-0614.

### Author Contributions

‡Contributed equally to this work.

## ACKNOWLEDGMENTS

This work is supported, in part, by the University of Wisconsin Carbone Cancer Center, the Department of Defense (W81XWH-11-1-0644 and W81XWH-11-1-0648), NCRR 1UL1RR025011, and the NIH through the UW Radiological Sciences Training Program 5 T32 CA009206-32.

## REFERENCES

(1) Hanahan, D.; Weinberg, R. A. Hallmarks of cancer: the next generation. *Cell* **2011**, *144*, 646–74.

(2) Carmeliet, P. Angiogenesis in life, disease and medicine. *Nature* **2005**, *438*, 932–6.

(3) Folkman, J. Angiogenesis in cancer, vascular, rheumatoid and other disease. *Nat. Med.* **1995**, *1*, 27–31.

(4) Cai, W.; Chen, X. Multimodality molecular imaging of tumor angiogenesis. *J. Nucl. Med.* **2008**, *49* (Suppl2), 113S–28S.

(5) Beer, A. J.; Schwaiger, M. Imaging of integrin $\alpha_v\beta_3$ expression. *Cancer Metastasis Rev.* **2008**, *27*, 631–44.

(6) Cai, W.; Chen, X. Multimodality imaging of vascular endothelial growth factor and vascular endothelial growth factor receptor expression. *Front. Biosci.* **2007**, *12*, 4267–79.

(7) Cai, W.; Niu, G.; Chen, X. Imaging of integrins as biomarkers for tumor angiogenesis. *Curr. Pharm. Des.* **2008**, *14*, 2943–73.

(8) Dijkgraaf, I.; Boerman, O. C. Radionuclide imaging of tumor angiogenesis. *Cancer Biother. Radiopharm.* **2009**, *24*, 637–47.

(9) Mittra, E. S.; Goris, M. L.; Iagaru, A. H.; Kardan, A.; Burton, L.; Berganos, R.; Chang, E.; Liu, S.; Shen, B.; Chin, F. T.; Chen, X.; Gambhir, S. S. Pilot pharmacokinetic and dosimetric studies of $^{18}$F-FPPRGD2: a PET radiopharmaceutical agent for imaging $\alpha_v$ $\beta_3$ integrin levels. *Radiology* **2011**, *260*, 182–91.

(10) Dallas, N. A.; Samuel, S.; Xia, L.; Fan, F.; Gray, M. J.; Lim, S. J.; Ellis, L. M. Endoglin (CD105): a marker of tumor vasculature and potential target for therapy. *Clin. Cancer Res.* **2008**, *14*, 1931–7.

(11) Fonsatti, E.; Nicolay, H. J.; Altomonte, M.; Covre, A.; Maio, M. Targeting cancer vasculature via endoglin/CD105: a novel antibody-based diagnostic and therapeutic strategy in solid tumours. *Cardiovasc. Res.* **2010**, *86*, 12–9.

(12) Seon, B. K.; Haba, A.; Matsuno, F.; Takahashi, N.; Tsujie, M.; She, X.; Harada, N.; Uneda, S.; Tsujie, T.; Toi, H.; Tsai, H.; Haruta, Y. Endoglin-targeted cancer therapy. *Curr. Drug Delivery* **2011**, *8*, 135–43.

(13) Fonsatti, E.; Altomonte, M.; Nicotra, M. R.; Natali, P. G.; Maio, M. Endoglin (CD105): a powerful therapeutic target on tumor-associated angiogenetic blood vessels. *Oncogene* **2003**, *22*, 6557–63.

(14) Yang, Y.; Zhang, Y.; Hong, H.; Liu, G.; Leigh, B. R.; Cai, W. In vivo near-infrared fluorescence imaging of CD105 expression. *Eur. J. Nucl. Med. Mol. Imaging* **2011**, *38*, 2066–76.

(15) Wikstrom, P.; Lissbrant, I. F.; Stattin, P.; Egevad, L.; Bergh, A. Endoglin (CD105) is expressed on immature blood vessels and is a marker for survival in prostate cancer. *Prostate* **2002**, *51*, 268–75.

(16) Fonsatti, E.; Jekunen, A. P.; Kairemo, K. J.; Coral, S.; Snellman, M.; Nicotra, M. R.; Natali, P. G.; Altomonte, M.; Maio, M. Endoglin is a suitable target for efficient imaging of solid tumors: *in vivo* evidence in a canine mammary carcinoma model. *Clin. Cancer Res.* **2000**, *6*, 2037–43.

(17) Bredow, S.; Lewin, M.; Hofmann, B.; Marecos, E.; Weissleder, R. Imaging of tumour neovasculature by targeting the TGF-beta binding receptor endoglin. *Eur. J. Cancer* **2000**, *36*, 675–81.

(18) Costello, B.; Li, C.; Duff, S.; Butterworth, D.; Khan, A.; Perkins, M.; Owens, S.; Al-Mowallad, A. F.; O'Dwyer, S.; Kumar, S. Perfusion of $^{99m}$Tc-labeled CD105 Mab into kidneys from patients with renal carcinoma suggests that CD105 is a promising vascular target. *Int. J. Cancer* **2004**, *109*, 436–41.

(19) Korpanty, G.; Carbon, J. G.; Grayburn, P. A.; Fleming, J. B.; Brekken, R. A. Monitoring response to anticancer therapy by targeting microbubbles to tumor vasculature. *Clin. Cancer Res.* **2007**, *13*, 323–30.

(20) Hong, H.; Yang, Y.; Zhang, Y.; Engle, J. W.; Barnhart, T. E.; Nickles, R. J.; Leigh, B. R.; Cai, W. Positron emission tomography imaging of CD105 expression during tumor angiogenesis. *Eur. J. Nucl. Med. Mol. Imaging* **2011**, *38*, 1335–43.

(21) Zhang, Y.; Hong, H.; Cai, W. PET tracers based on Zirconium-89. *Curr. Radiopharm.* **2011**, *4*, 131–9.

(22) Massoud, T. F.; Gambhir, S. S. Molecular imaging in living subjects: seeing fundamental biological processes in a new light. *Genes Dev.* **2003**, *17*, 545–80.

(23) Zhang, Y.; Hong, H.; Engle, J. W.; Yang, Y.; Barnhart, T. E.; Cai, W. Positron emission tomography and near-infrared fluorescence imaging of vascular endothelial growth factor with dual-labeled bevacizumab. *Am. J. Nucl. Med. Mol. Imaging* **2012**, *2*, 1–13.

(24) Frangioni, J. V. *In vivo* near-infrared fluorescence imaging. *Curr. Opin. Chem. Biol.* **2003**, *7*, 626−34.
(25) Cai, W.; Hsu, A. R.; Li, Z. B.; Chen, X. Are quantum dots ready for *in vivo* imaging in human subjects? *Nanoscale Res. Lett.* **2007**, *2*, 265−81.
(26) Mendelson, D. S.; Gordon, M. S.; Rosen, L. S.; Hurwitz, H.; Wong, M. K.; Adams, B. J.; Alvarez, D.; Seon, B. K.; Theuer, C. P.; Leigh, B. R. Phase I study of TRC105 (anti-CD105 [endoglin] antibody) therapy in patients with advanced refractory cancer. *J. Clin. Oncol.* **2010**, *28*, 15s.
(27) Wang, H.; Cai, W.; Chen, K.; Li, Z. B.; Kashefi, A.; He, L.; Chen, X. A new PET tracer specific for vascular endothelial growth factor receptor 2. *Eur. J. Nucl. Med. Mol. Imaging* **2007**, *34*, 2001−2010.
(28) Takahashi, N.; Haba, A.; Matsuno, F.; Seon, B. K. Antiangiogenic therapy of established tumors in human skin/severe combined immunodeficiency mouse chimeras by anti-endoglin (CD105) monoclonal antibodies, and synergy between anti-endoglin antibody and cyclophosphamide. *Cancer Res.* **2001**, *61*, 7846−54.
(29) Cai, W.; Wu, Y.; Chen, K.; Cao, Q.; Tice, D. A.; Chen, X. *In vitro* and *in vivo* characterization of $^{64}$Cu-labeled Abegrin$^{TM}$, a humanized monoclonal antibody against integrin $\alpha_v\beta_3$. *Cancer Res.* **2006**, *66*, 9673−81.
(30) Cai, W.; Chen, K.; Mohamedali, K. A.; Cao, Q.; Gambhir, S. S.; Rosenblum, M. G.; Chen, X. PET of vascular endothelial growth factor receptor expression. *J. Nucl. Med.* **2006**, *47*, 2048−56.
(31) Maeda, H.; Wu, J.; Sawa, T.; Matsumura, Y.; Hori, K. Tumor vascular permeability and the EPR effect in macromolecular therapeutics. A review. *J. Controlled Release* **2000**, *65*, 271−84.
(32) Tanaka, T.; Shiramoto, S.; Miyashita, M.; Fujishima, Y.; Kaneo, Y. Tumor targeting based on the effect of enhanced permeability and retention (EPR) and the mechanism of receptor-mediated endocytosis (RME). *Int. J. Pharm.* **2004**, *277*, 39−61.
(33) van Dam, G. M.; Themelis, G.; Crane, L. M.; Harlaar, N. J.; Pleijhuis, R. G.; Kelder, W.; Sarantopoulos, A.; de Jong, J. S.; Arts, H. J.; van der Zee, A. G.; Bart, J.; Low, P. S.; Ntziachristos, V. Intraoperative tumor-specific fluorescence imaging in ovarian cancer by folate receptor-alpha targeting: first in-human results. *Nat. Med.* **2011**, *17*, 1315−9.
(34) Cai, W.; Ebrahimnejad, A.; Chen, K.; Cao, Q.; Li, Z. B.; Tice, D. A.; Chen, X. Quantitative radioimmunoPET imaging of EphA2 in tumor-bearing mice. *Eur. J. Nucl. Med. Mol. Imaging* **2007**, *34*, 2024−36.
(35) Eary, J. F.; Hawkins, D. S.; Rodler, E. T.; Conrad, E. U. I. $^{18}$F-FDG PET in sarcoma treatment response imaging. *Am. J. Nucl. Med. Mol. Imaging* **2011**, *1*, 47−53.
(36) Gambhir, S. S.; Czernin, J.; Schwimmer, J.; Silverman, D. H.; Coleman, R. E.; Phelps, M. E. A tabulated summary of the FDG PET literature. *J. Nucl. Med.* **2001**, *42*, 1S−93S.
(37) Grassi, I.; Nanni, C.; Allegri, V.; Morigi, J. J.; Montini, G. C.; Castellucci, P.; Fanti, S. The clinical use of PET with $^{11}$C-acetate. *Am. J. Nucl. Med. Mol. Imaging* **2012**, *2*, 33−47.
(38) Alauddin, M. M. Positron emission tomography (PET) imaging with $^{18}$F-based radiotracers. *Am. J. Nucl. Med. Mol. Imaging* **2012**, *2*, 55−76.
(39) Vach, W.; Høilund-Carlsen, P. F.; Fischer, B. M.; Gerke, O.; Weber, W. How to study optimal timing of PET/CT for monitoring of cancer treatment. *Am. J. Nucl. Med. Mol. Imaging* **2011**, *1*, 54−62.
(40) Wadas, T. J.; Wong, E. H.; Weisman, G. R.; Anderson, C. J. Coordinating radiometals of copper, gallium, indium, yttrium, and zirconium for PET and SPECT imaging of disease. *Chem. Rev.* **2010**, *110*, 2858−902.
(41) Dearling, J. L. J.; Voss, S. D.; Dunning, P.; Snay, E.; Fahey, F.; Smith, S. V.; Huston, J. S.; Meares, C. F.; Treves, S. T.; Packard, A. B. Imaging cancer using PET -- the effect of the bifunctional chelator on the biodistribution of a $^{64}$Cu-labeled antibody. *Nucl. Med. Biol.* **2011**, *38*, 29−38.